

A CASE AGAINST SPINNING PAHS AS THE SOURCE OF THE ANOMALOUS MICROWAVE EMISSION

BRANDON S. HENSLEY AND B. T. DRAINE

Department of Astrophysical Sciences, Princeton University, Princeton, NJ 08544, USA

(Dated: January 27, 2023)

Draft version January 27, 2023

ABSTRACT

We employ the all-sky map of the anomalous microwave emission (AME) produced by component separation of the microwave sky to study correlations between the AME and Galactic dust properties. We find that while the AME is highly correlated with all tracers of dust emission, fluctuations in the AME intensity per dust optical depth are uncorrelated with fluctuations in the emission from polycyclic aromatic hydrocarbons (PAHs), casting doubt on the association between AME and PAHs. Further, we find that the best predictor of the AME strength is the dust radiance and that the AME intensity increases with increasing radiation field strength, at variance with predictions from the spinning dust hypothesis. A reconsideration of other emission mechanisms, such as magnetic dipole emission, is warranted.

Subject headings: ISM: dust, extinction— diffuse radiation— radio continuum: ISM— radiation mechanisms: general

1. INTRODUCTION

High sensitivity, full-sky observations of the far-infrared and microwave sky from WMAP and *Planck* have pushed studies of the Cosmic Microwave Background (CMB) to a regime in which contamination from Galactic foregrounds has become a key uncertainty in the analysis. Understanding the physical nature of the foreground components and producing better models of each are essential for mitigating this uncertainty.

The anomalous microwave emission (AME) is perhaps the least well-understood of the foreground components. Discovered as a dust-correlated emission excess peaking near 30 GHz (Kogut et al. 1996; de Oliveira-Costa et al. 1997; Leitch et al. 1997), AME is often ascribed to electric dipole emission from rapidly rotating ultrasmall dust grains (Draine & Lazarian 1998a,b; Hoang et al. 2010; Ysard & Verstraete 2010; Silsbee et al. 2011), i.e. “spinning dust emission.” Empirically, this emission component peaks between ~ 20 and 50 GHz (e.g. Planck Collaboration et al. 2014b) and has an emissivity per H of $\sim 3 \times 10^{-18} \text{ Jy sr}^{-1} \text{ cm}^2 \text{ H}^{-1}$ at 30 GHz (Dobler et al. 2009; Tibbs et al. 2010, 2011; Planck Collaboration et al. 2014b,c). Polycyclic aromatic hydrocarbons (PAHs), which give rise to prominent emission features in the infrared, have been suggested as the source of the AME due to their small size and apparent abundance.

Theoretical spinning dust SED templates have been successful in fitting observations both in the Galaxy (Miville-Deschénes et al. 2008; Hoang et al. 2011; Planck Collaboration et al. 2015b) and in the sole extragalactic detection in the star-forming galaxy NGC 6946 (Murphy et al. 2010; Scaife et al. 2010; Hensley et al. 2015).

The AME has been observed to correlate well with the PAH emission features in the infrared. Ysard et al. (2010) showed that, over the full sky, the AME was more correlated with emission at $12 \mu\text{m}$ than with $100 \mu\text{m}$. Likewise, the AME in the dark cloud LDN 1622 was better correlated with the 12 and $25 \mu\text{m}$ emission than with

either the 60 or $100 \mu\text{m}$ emission (Casassus et al. 2006). However, studying the AME in a sample of 98 Galactic clouds, Planck Collaboration et al. (2014b) found no significant differences between the 12 , 25 , 60 , and $100 \mu\text{m}$ emission in their correlation with the AME. Additionally, the link between the AME and PAH abundance determined from dust model fitting has proven tenuous in NGC 6946 (Hensley et al. 2015).

In addition to spinning ultrasmall grains, grains containing ferro- or ferrimagnetic materials are also predicted to radiate strongly in the microwave and may contribute to the AME (Draine & Lazarian 1999; Draine & Hensley 2013). Draine & Lazarian (1999) argued that the spinning dust and magnetic emission mechanisms could be distinguished by observing the AME in dense regions where PAHs would likely be depleted due to coagulation. If the AME per dust mass is constant across both dense and diffuse regions, then spinning dust emission would be disfavored.

In this work, we test the spinning dust hypothesis using new full-sky observations of the infrared and microwave sky. Planck Collaboration et al. (2015b) decomposed the *Planck* sky into foreground components making use of both the 9-year WMAP data and the Haslam 408 MHz survey. The combination of these data allowed the low frequency foreground components – primarily synchrotron, free-free, and AME – to be disentangled, producing a full-sky map of the AME.

All-sky WISE observations at $12 \mu\text{m}$, a tracer of PAH emission, have natural synergy with the AME map, allowing us to test at high significance the link between the AME and PAHs. Additionally, all-sky dust modeling by Planck Collaboration et al. (2014a) permits deeper exploration into the dust and environmental parameters that influence the strength of the AME.

This paper is organized as follows: in Section 2 we summarize the data sets used in our analysis; in Section 3 we describe the correlations predicted by our current understanding of the spinning dust hypothesis; in Section 4 we present the relationships between environmental and

dust properties and AME as derived from the data; in Section 5 we discuss the implications of these results on spinning dust theory in particular and AME modeling in general; and we summarize our principal conclusions in Section 6.

2. DATA

2.1. *Planck* Foreground Separation Maps

Combining full-mission all-sky *Planck* observations (Planck Collaboration et al. 2015a) with the 9-yr. WMAP data (Bennett et al. 2013) and the Haslam 408 MHz survey (Haslam et al. 1982), Planck Collaboration et al. (2015b) used data from 32 different detectors spanning a range of 408 MHz to 857 GHz in frequency to perform foreground component separation within the Bayesian **Commander** analysis framework (Eriksen et al. 2004, 2006, 2008). They constructed theoretically-motivated models for the frequency dependence of each component – including the CMB, synchrotron, free-free, thermal dust, and AME – while minimizing the number of free parameters needed and simultaneously fitting for calibration offsets. Using a Gibbs sampling algorithm, they determined the best-fit values for each model parameter on a pixel-by-pixel basis.

In this work, we focus primarily upon the resulting map of the AME. This component was modeled by the sum of *two* spinning dust spectra with fixed spectral shape as determined by the **SpDust** code (Ali-Haïmoud et al. 2009; Silsbee et al. 2011), but differing amplitudes and peak frequencies. One of the spectra was required to have a spatially fixed peak frequency, fit to be 33.35 GHz, while the other peak frequency was allowed to freely vary from pixel to pixel. Thus, the data products consist of an amplitude for each AME component, the peak frequency of the spatially varying component, and the uncertainty of each for every pixel on the sky.

To facilitate comparisons with the literature, we calculate the sum of the two components at 30 GHz. We also calculate the uncertainty in this quantity assuming Gaussian errors and ignoring the uncertainty on the peak frequency of both components.

In addition to the AME map, we employ the parameters from the thermal dust fit to compute the 353 GHz dust optical depth τ_{353} . Although this parameter was also an explicit data product of the full-sky modified blackbody fits performed by Planck Collaboration et al. (2014a), we prefer to use the results from Planck Collaboration et al. (2015b) for several reasons. First, the fits were performed on more data and with more detailed treatment of calibration and bandpass uncertainties. Second, the fits were performed at 1° versus $5'$ resolution, mitigating the effects of cosmic infrared background (CIB) anisotropies. Finally, the modified blackbody model has been demonstrated to break down when extrapolated from *Planck* HFI frequencies to $100\,\mu\text{m}$ (Planck Collaboration et al. 2015b). Thus, we prefer to use a τ_{353} derived from fits to the Rayleigh-Jeans portion of the dust emission spectrum only. We find τ_{353} derived in this way to be on average 10% lower than that reported by Planck Collaboration et al. (2014a).

Additionally we employ the parameter maps that characterize the free-free, synchrotron, and CO emission. As free-free and CO emission cannot be fit reliably in regions

of low surface brightness, we exclude all pixels with emission measure of $0.1\,\text{cm}^{-6}\,\text{pc}$ or less and with no fit CO emission when analyzing the former and latter, respectively.

The **Commander** parameter maps employed in this study have a resolution of 1° and are pixellated with **HEALPix** (Górski et al. 2005) resolution of $N_{\text{side}} = 256$, i.e. about $13'.7$ on a side.

2.2. *Dust Parameter Maps from Modified Blackbody Fitting*

A key limitation of the thermal dust fits performed by Planck Collaboration et al. (2015b) is the omission of any data at higher frequency than the *Planck* 857 GHz band. Without information on the Wien side of the dust emission spectrum, it is difficult to constrain the dust temperature and luminosity.

Thus, we employ the full-sky parameter maps of Planck Collaboration et al. (2014a), who fit a modified blackbody model of the dust emission to the 2013 *Planck* 857, 545, and 353 GHz data as well as $100\,\mu\text{m}$ data from IRAS. For the latter, they employ both the reprocessed IRIS map (Miville-Deschénes & Lagache 2005) as well as the map of Schlegel et al. (1998). The fits were performed at $5'$ resolution and yielded an estimate of τ_{353} , the dust radiance \mathcal{R} , the dust temperature T_d , and the dust spectral index β for each pixel. We employ \mathcal{R} , T_d , and β from these fits in our analysis, but use τ_{353} from the **Commander** fits as discussed above.

We use the parameter map pixellated with **HEALPix** resolution of $N_{\text{side}} = 2048$, then downgrade the resolution to $N_{\text{side}} = 256$.

2.3. *WISE* $12\,\mu\text{m}$ Map

WISE observed the full sky in four infrared bands – 3.4 , 4.6 , 12 , and $22\,\mu\text{m}$ (Wright et al. 2010). The $12\,\mu\text{m}$ band captures the strongest of the infrared emission features associated with PAHs and thus traces the population of small dust grains. We employ the WISE $12\,\mu\text{m}$ map reprocessed by Meisner & Finkbeiner (2014), who performed point source subtraction, destriping, and removal of time-dependent foregrounds on the official WISE data products. We use their map pixellated with **HEALPix** resolution of $N_{\text{side}} = 1024$, then downgrade the resolution to $N_{\text{side}} = 256$.

2.4. *IRIS* $100\,\mu\text{m}$ Map

Following Planck Collaboration et al. (2014a), we employ the reprocessed IRAS $100\,\mu\text{m}$ IRIS maps (Miville-Deschénes & Lagache 2005), though we do not apply the additional large-scale filtering as described in Planck Collaboration et al. (2014a). The IRIS maps were downgraded from $N_{\text{side}} = 1024$ to 256.

2.5. Masks

While PAHs are typically the dominant contributors of the $12\,\mu\text{m}$ emission, zodiacal light can also contribute significantly at this wavelength and thus bias our primary PAH tracer. We therefore exclude all pixels within five degrees of the ecliptic plane (8.7% of the sky) to mitigate this effect.

Likewise, artifacts from moon contamination are also present in the $12\,\mu\text{m}$ map. We therefore mask all pixels

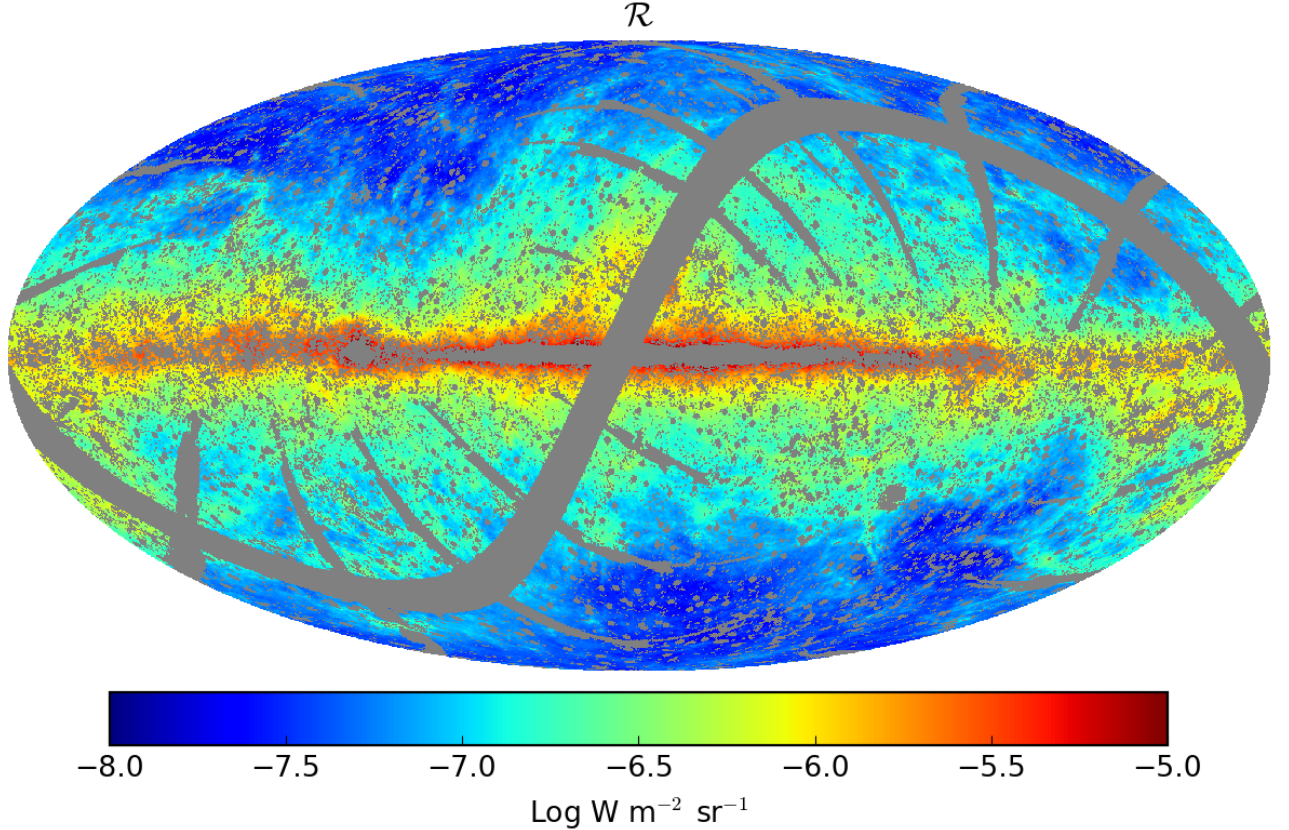


FIG. 1.— The Mollweide projection full-sky map of \mathcal{R} as derived by Planck Collaboration et al. (2014a) with the mask described in Section 2.5 overlaid in gray.

flagged for moon contamination by Meisner & Finkbeiner (2014), totaling 5.9% of the sky.

To mitigate the effects of point sources, we employ the *Planck* point source masks in intensity at each HFI¹ and LFI² band (Planck Collaboration et al. 2015a). These masks eliminate point sources with signal-to-noise greater than 5 at resolution $N_{\text{side}} = 2048$. We downgrade these masks to $N_{\text{side}} = 256$, resulting in a total of 23% of the sky being masked.

Finally, we use the *Planck* Galactic plane mask covering 1% of the sky based on the 353 GHz HFI data³ (Planck Collaboration et al. 2015a). This eliminates the regions in the Galactic plane with the most complicated and highest intensity emission and where the relatively simple foreground models are most likely to break down.

After applying the masks described above, 603,242 pixels covering 65% of the sky remain. The total mask is illustrated in Figure 1 on the full-sky \mathcal{R} map. This combination of masks is used in all analysis, although we discuss the sensitivity of our results to various additional masking (e.g. masking the Galactic plane) in Section 4.6.

3. TESTS OF AME THEORY

¹ http://irsa.ipac.caltech.edu/data/Planck/release_2/ancillary-data/masks/HFI_Mask_PointSrc_2048_R2.00.fits

² http://irsa.ipac.caltech.edu/data/Planck/release_2/ancillary-data/masks/LFI_Mask_PointSrc_2048_R2.00.fits

³ http://irsa.ipac.caltech.edu/data/Planck/release_2/ancillary-data/masks/HFI_Mask_GalPlane-apo0_2048_R2.00.fits

3.1. AME Theory

The AME has been suggested to be electric dipole emission from ultrasmall, rapidly-rotating grains that have been torqued up through interactions with both the gas and radiation field (Draine & Lazarian 1998b; Hoang et al. 2010; Ysard & Verstraete 2010; Silsbee et al. 2011). The observed peak frequency of the emission requires that the grains be small (radius $a \lesssim 10 \text{ \AA}$), leading to a natural association with the PAHs that produce emission features in the infrared.

If so, we might expect a linear relation between the total PAH surface density Σ_{PAH} and the AME intensity. Adopting an empirical 30 GHz spinning dust emissivity of $3 \times 10^{-18} \text{ Jy sr}^{-1} \text{ cm}^2 \text{ H}^{-1}$, and assuming this corresponds to typical Galactic values of $M_d/M_H = 0.0078$ and $\Sigma_{\text{PAH}}/\Sigma_d = 0.046$ (Draine & Li 2007), we would expect

$$I_{\nu, 30 \text{ GHz}}^{\text{AME}} = 1.0 \left(\frac{\Sigma_{\text{PAH}}}{M_{\odot} \text{ kpc}^{-2}} \right) \text{ Jy sr}^{-1} . \quad (1)$$

In the context of the spinning dust model, environmental factors can influence both the peak frequency of the emission and the emissivity itself. The importance of collisions with ions depends on the fractional ionization and the charge state of the ultrasmall grains. In regions with very intense radiation fields, drag forces from IR photon emission become important. Damping by the rotational emission generally causes the ultrasmall grains to have sub-LTE rotation rates.

The electric dipole moment distribution of the dust population will also strongly influence the emissivity, though we have no *a priori* estimates of the systematic variations of this quantity from one region to another.

We expect spinning dust emission to be relatively insensitive to the strength of the radiation field, which is an important source of excitation only in fairly extreme environments such as reflection nebulae and photo-dissociation regions (PDRs). However, the emissivity per unit gas mass should increase with increasing local gas density, which may correlate with the radiation field strength.

The impact of these factors on the 30 GHz AME flux density was estimated by Draine & Lazarian (1998b) to be only about a factor of two between the Cold Neutral Medium, Warm Neutral Medium, and Warm Ionized Medium environments. In our study, these effects are mitigated by the low angular resolution of the maps, which are likely to be sampling dust emission from different environments within each pixel.

These caveats notwithstanding, the spinning PAH model for the AME predicts:

1. A linear correlation of the PAH surface density and the AME flux density at 30 GHz.
2. Relatively constant AME per PAH surface density over a range of radiation field strengths.

3.2. Data Model

τ_{353} is equal to the product of the dust mass column density and the dust opacity at 353 GHz. Because dust grains are much smaller than the wavelength of light at this frequency, the dust opacity is insensitive to the size distribution of the grains and τ_{353} is thus a reliable indicator of the dust column density. There is evidence, however, that the dust optical properties change somewhat in different environments (Plank Collaboration et al. 2014).

The dust radiance \mathcal{R} is the frequency-integrated dust intensity for the best-fit single temperature modified blackbody with $\tau_\nu \propto \nu^\beta$, and is thus a tracer of both the dust column density and the strength of the radiation field heating the dust.

Finally, the 12 μm flux density is effectively a measure of the total power emitted by PAHs, i.e. the starlight power absorbed by PAHs. Thus, the ratio of the 12 μm emission to the dust radiance is a proxy for the fraction of dust in PAHs. For the purposes of this work, we define

$$f_{\text{PAH}} \equiv \frac{(\nu I_\nu)^{12 \mu\text{m}}}{\mathcal{R}} . \quad (2)$$

The product $f_{\text{PAH}}\tau_{353}$ is then a proxy for the PAH column density. It is this quantity which the spinning dust model predicts to be the most accurate predictor of the strength of the AME.

We assume that each of the dust observables discussed above correlate with the AME intensity in a linear way, i.e., for each pixel i and each observable A_i , the AME intensity in that pixel is given simply by $\alpha_i A_i$ where α_i is a constant to be determined.

To identify the physical quantity which is the best predictor of the AME intensity, we wish to quantify the intrinsic dispersion in α_i across all pixels. We assume that

TABLE 1
CORRELATION ANALYSIS
 $I_{\nu, 30 \text{ GHz}}^{\text{AME}} = \alpha A$

A	$\alpha \pm \sigma_\alpha$	σ_α/α
$I_\nu^{12 \mu\text{m}}$	$(6.51 \pm 1.99) \times 10^{-3}$	0.31
\mathcal{R}	$\frac{5320 \pm 1720}{\text{W m}^{-2} \text{sr}^{-1}} \text{ MJy sr}^{-1}$	0.32
τ_{353}	$189 \pm 76 \text{ MJy sr}^{-1}$	0.40
$f_{\text{PAH}}\tau_{353}$	$939 \pm 415 \text{ MJy sr}^{-1}$	0.44
$I_\nu^{100 \mu\text{m}}$	$(1.89 \pm 0.88) \times 10^{-4}$	0.46

NOTE. — α and σ_α are the best fit values obtained from Equation 3 for each observable A such that $I_{\nu, 30 \text{ GHz}}^{\text{AME}} = \alpha A$. The formal uncertainties on α and σ_α are less than the quoted accuracy in the table, generally of order 0.1%.

each pixel samples a Gaussian distribution with mean α and standard deviation σ_α .

The likelihood of this model given the data over all pixels is:

$$\mathcal{L} \propto \prod_i \frac{1}{\sqrt{\sigma_{I,i}^2 + (A_i \sigma_\alpha)^2}} \times \exp \left[\frac{-(I_{\nu, 30 \text{ GHz},i}^{\text{AME}} - \alpha A_i)^2}{\sigma_{I,i}^2 + (A_i \sigma_\alpha)^2} \right] , \quad (3)$$

where $\sigma_{I,i}$ is the uncertainty on $I_{\nu, 30 \text{ GHz},i}^{\text{AME}}$. We thus seek the maximum likelihood values of α and σ_α for each observable A . In practice, we employ the `emcee` Markov chain Monte Carlo code (Foreman-Mackey et al. 2013) to derive the best fit values and confidence intervals for each parameter assuming uninformative priors.

In addition to the uncertainties described above, each observable A also has an associated observational uncertainty σ_A which we have not included in Equation 3. To assess the impact of neglecting this error term, we performed a second analysis as follows. Because many of the observables were derived from model fits and often from data at higher resolution than the `Commander` maps, quantifying σ_A accurately is difficult. Therefore, we fit this quantity empirically by assuming σ_A in each pixel is directly proportional to A where the constant of proportionality is the same for all pixels. We find that while including this error term tends to decrease our estimate for σ_α , the overall ordering of the observables by σ_α is unchanged. Therefore, our conclusions do not appear sensitive to the relative precision with which each observable was determined.

4. RESULTS

4.1. Correlation with PAH Abundance

We test the predictions of the spinning PAH hypothesis laid out in Section 3.1 by relating the observational data to physical properties of the dust through the model described in Section 3.2.

In Figure 2 we plot the AME flux density at 30 GHz against τ_{353} , $f_{\text{PAH}}\tau_{353}$, the dust radiance \mathcal{R} , and the 100 μm flux density $I_\nu^{100 \mu\text{m}}$. All four correlate highly with AME as expected, and we present the fit slope of the relation with each in Table 1. The tightness of each correlation is indicated by σ_α/α , with $I_\nu^{12 \mu\text{m}}$ and \mathcal{R} having the smallest values.

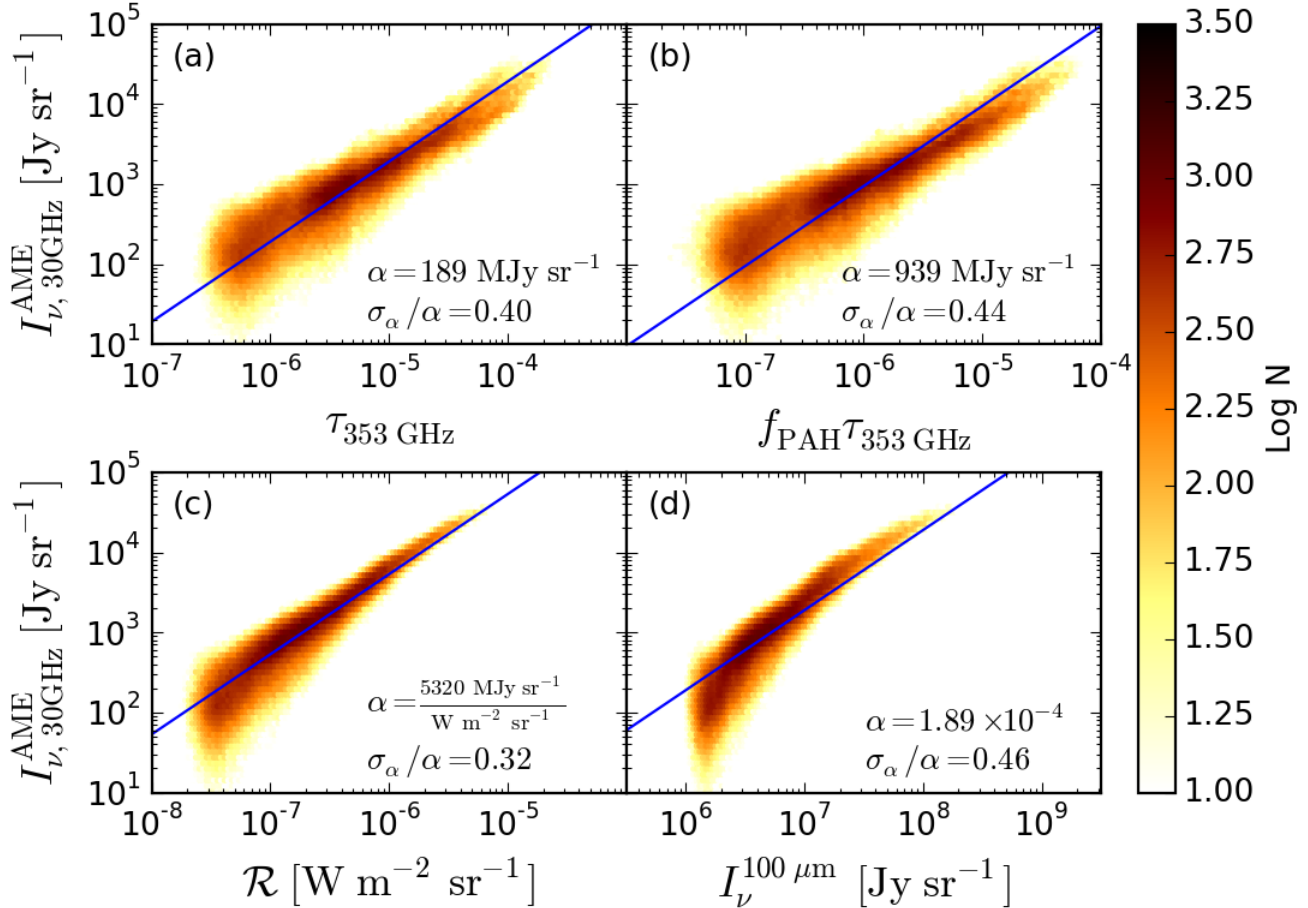


FIG. 2.— The 30 GHz AME intensity is plotted against (a) τ_{353} , (b) $f_{\text{PAH}}\tau_{353}$, (c) \mathcal{R} , and (d) $I_{\nu}^{100\mu\text{m}}$. We divide the plot area into hexagons of equal area in log-space and color each according to the number of pixels that fall within that hexagon. Each panel has the same logarithmic area allowing for straightforward comparisons between panels. In doing this, we have restricted the range of each plot to exclude some outlying points. In each panel we also plot (solid blue) the line with slope equal to the best-fit value of α . All four quantities are excellent tracers of the AME, but it is clear that \mathcal{R} traces the AME with the greatest fidelity and least dispersion.

If the AME arises from spinning PAHs, we would expect the emission to correlate better with $f_{\text{PAH}}\tau_{353}$ than τ_{353} . While it is clear that both are good tracers of AME, τ_{353} has a smaller dispersion about the best-fit relation than $f_{\text{PAH}}\tau_{353}$. Maximizing Equation 3, $A = \tau_{353}$ yields a relation with $\sigma_{\alpha}/\alpha = 0.40$ while $A = f_{\text{PAH}}\tau_{353}$ yields $\sigma_{\alpha}/\alpha = 0.44$ (see Table 1). Thus, f_{PAH} does not appear to contain additional information about the strength of the AME not already present in τ_{353} .

The spinning PAH model predicts that variations in the AME intensity per unit dust mass should arise from variations in the abundance of small grains. Therefore, as a second test of the link between the AME and PAHs, we look for correlations between f_{PAH} and the AME per τ_{353} .

In Figure 3a we plot the AME intensity normalized by $\alpha\tau_{353}$ against f_{PAH} , but we find no robust evidence for a correlation. We quantify this with the Spearman rank correlation coefficient r_s which, unlike the Pearson correlation coefficient, does not assume a functional form for the relationship between the two variables. We find $r_s = -0.18$, suggesting no correlation or even weak anti-correlation. Quantifying the correlation between f_{PAH} and the AME intensity normalized instead by $\alpha\mathcal{R}$ (see Figure 3b) yields $r_s = 0.19$, roughly the same value but

of opposite sign. Thus fluctuations in PAH abundance appear unable to account for the observed variations in the AME per dust mass and AME per dust radiance.

We note that f_{PAH} is itself correlated with both τ_{353} and \mathcal{R} as demonstrated in Figure 4, arguing strongly for PAH destruction in the diffuse ISM (low τ_{353}). The depletion of PAHs by a factor of ~ 3 to suppress photoelectric heating in the warm ionized medium (WIM) has been invoked to explain high ratios of H α to free-free emission (Dong & Draine 2011) and is consistent with the range of f_{PAH} we observe.

A study of the H α -correlated AME by Dobler et al. (2009) found the AME to be a factor of ~ 3 less intense than the amplitude calculated by Draine & Lazarian (1998a,b) and suggested that this discrepancy was due to PAH depletion in the WIM. However, subsequent studies have suggested an AME amplitude a factor of ~ 3 lower than the earlier estimates even in Galactic clouds (Tibbs et al. 2010, 2011; Planck Collaboration et al. 2014b,c). Thus, the results of Dobler et al. (2009) indicate instead a robustness of the AME strength across environments and, together with our results, further evidence that the AME is not associated with PAHs.

Figure 4 illustrates that f_{PAH} varies only from $\sim 0.15 - 0.25$ over most of the sky, suggesting that vari-

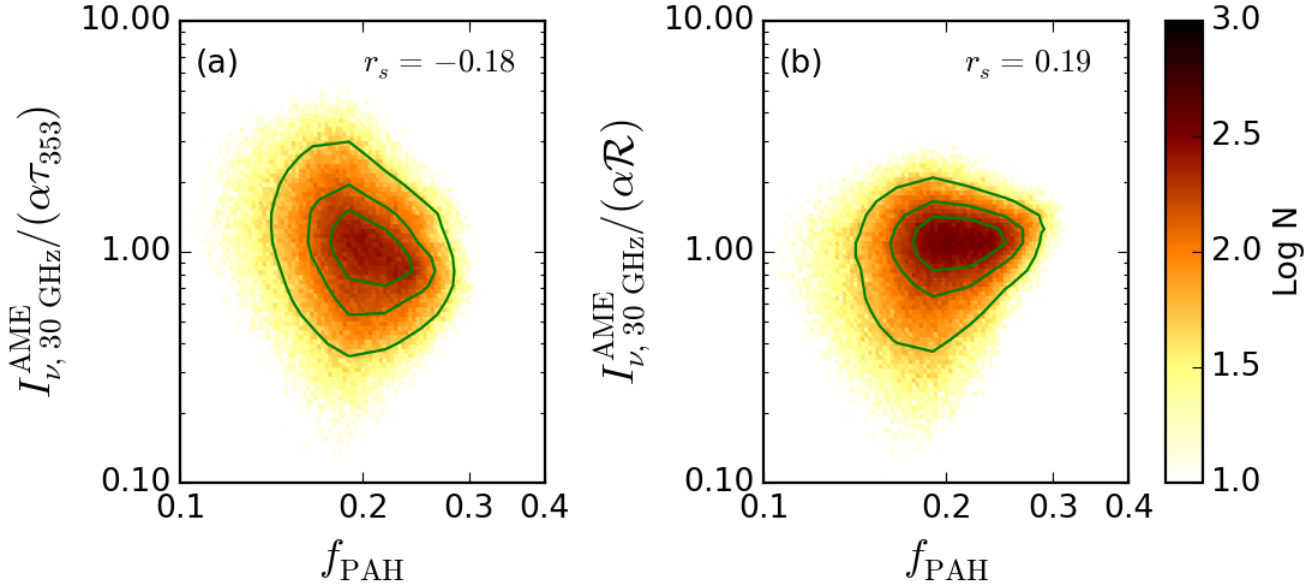


FIG. 3.— f_{PAH} is plotted against the AME intensity normalized by (a) $\alpha\tau_{353}$ and (b) $\alpha\mathcal{R}$. The isodensity contours corresponding to 25, 50, and 75% of the pixels enclosed are plotted in green. There is no apparent correlation between f_{PAH} and the AME, at variance with the spinning PAH hypothesis.

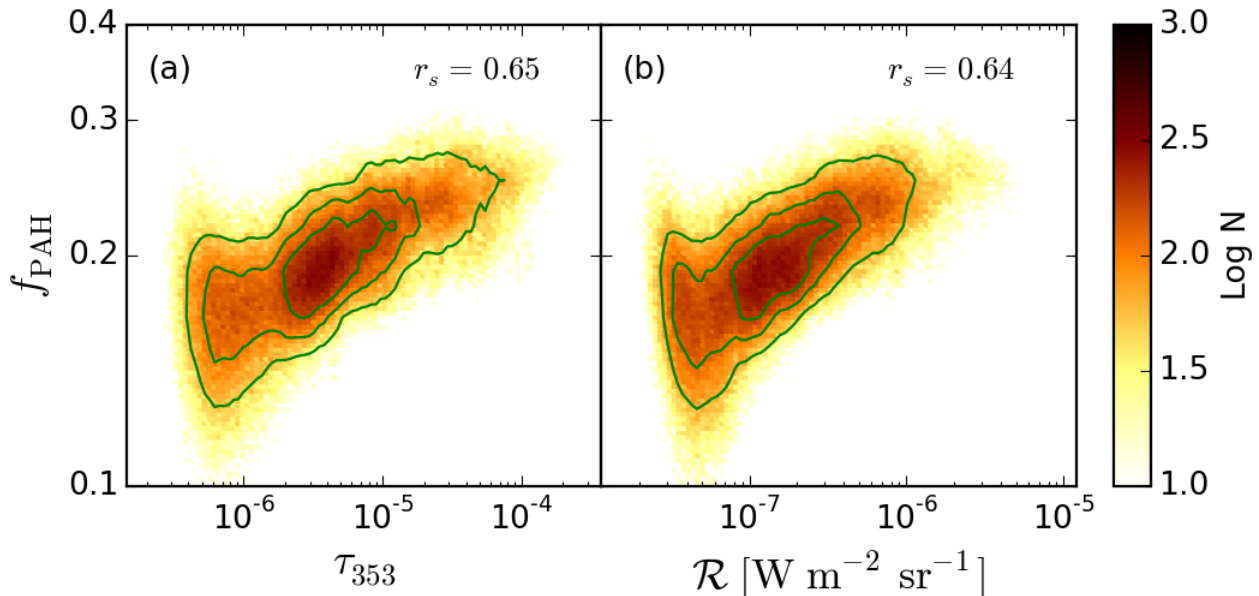


FIG. 4.— Plotting f_{PAH} against both (a) τ_{353} and (b) \mathcal{R} , it is clear that a strong positive correlation is present with both, consistent with depletion of PAHs in the diffuse ISM. The majority of the pixels have $0.15 < f_{\text{PAH}} < 0.25$, suggesting that fluctuations in PAH abundance could account for a scatter of a factor of at most ~ 1.5 in AME intensity unit per dust mass.

ations in the PAH abundance can account for no more than a factor of ~ 1.5 dispersion in AME intensity per dust mass.

Figures 2a and 5c demonstrate that $\alpha\tau_{353}$ tends to underpredict the true AME intensity at low values of τ_{353} and to overpredict at high values. Since f_{PAH} is positively correlated with τ_{353} , it is not surprising that assuming a linear relationship between the AME and $f_{\text{PAH}}\tau_{353}$ only exacerbates those discrepancies.

4.2. Correlation with the Radiation Field

Figure 2 and Table 1 also indicate the surprising result that the AME is more tightly correlated with \mathcal{R} than τ_{353} . We would expect \mathcal{R} and τ_{353} to be related through the strength of the radiation field— a fixed quantity of dust will radiate more when exposed to more radiation. The most straightforward conclusion is that the AME is enhanced by a stronger radiation field, which runs counter to the predictions of the spinning dust hypothesis (Ali-Haïmoud et al. 2009; Ysard & Verstraete 2010).

In Figure 5a, we investigate this possibility by performing the same test as with f_{PAH} , looking now for

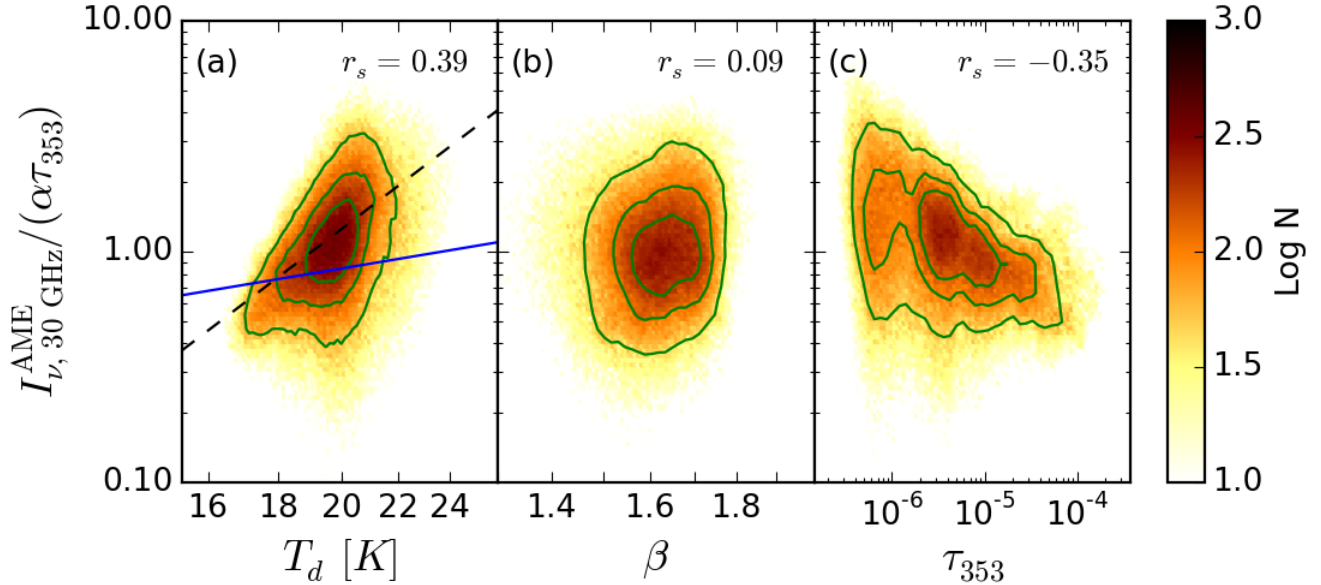


FIG. 5.— The 30 GHz AME intensity normalized by $\alpha\tau_{353}$ is plotted against (a) T_d and (b) β determined by modified blackbody fits to the dust SED (Planck Collaboration et al. 2014a), and against τ_{353} determined from component separation (Planck Collaboration et al. 2015b) in panel (c). Since PAHs are depleted in dense regions, the spinning PAH hypothesis predicts that the AME per τ_{353} should be smaller in denser regions. These regions are likely to have more cold dust and thus a smaller β , but no correlation is observed between β and the AME intensity per τ_{353} . However, there is robust correlation with T_d , suggesting either sensitivity of the AME to the radiation field or else environmental conditions that correlate with stronger radiation. To quantify the relationship, we derive a best-fit power-law of $T^{4.53}$ (black dashed) and plot also the best fit linear relation (blue solid). The linear relationship, as would be expected from thermal emission in the Rayleigh-Jeans limit, is strongly disfavored.

correlations between T_d and the AME intensity normalized by $\alpha\tau_{353}$. We find evidence of a positive correlation ($r_s = 0.39$), suggesting that indeed the AME is stronger *per unit dust mass* in regions with more intense radiation fields and thus warmer dust.

A positive correlation between the radiation field strength and the AME intensity was also noted by Planck Collaboration et al. (2014b). They attribute the correlation to a positive correlation between the radiation field and the local gas density.

The relationship between the AME/τ_{353} and T_d in 5a is best-fit by a power-law of index 4.53. If the AME were thermal emission in the Rayleigh-Jeans limit, we would expect a linear scaling with T_d . While the temperature T_{AME} of the AME-emitting grains may differ from the T_d characterizing the dominant FIR-submillimeter emission, it would be surprising for T_{AME} to increase by a factor of ~ 3 when T_d varies only from 17 to 22 K.

If the fit AME component is contaminated with emission from other low-frequency foregrounds, then this may also induce correlations with T_d . We discuss this possibility further in Section 5, though contamination appears to be minimal.

For pixels containing regions with both high and low radiation intensities, fitting the $\lambda \geq 100 \mu\text{m}$ emission by a single-temperature modified blackbody will lead to systematic errors, tending to overestimate T_d and underestimate both β and τ_{353} . Thus, if the correlation between the AME and the dust radiance is driven by the correlation between the radiation field intensity and the local gas density, we might expect the AME per τ_{353} to correlate with β . We find no evidence for such a correlation (see Figure 5b). Likewise, we find no compelling evidence for a strong correlation between the AME and CO

emission (see Figure 8c).

4.3. Correlation with $I_{\nu}^{100 \mu\text{m}}$

The ratio of the 30 GHz and $100 \mu\text{m}$ flux densities is often quoted in the literature. We obtain a value of $(1.89 \pm 0.88) \times 10^{-4}$ (see Table 1), consistent with other determinations in the literature. For instance, performing component separation on WMAP observations at intermediate Galactic latitudes, Davies et al. (2006) derived a ratio of 3×10^{-4} . Alves et al. (2010) likewise find a ratio of 3×10^{-4} combining observations of radio recombination lines in the Galactic plane with WMAP data. Studying HII regions in the Galactic plane with the Very Small Array at 33 GHz, Todorović et al. (2010) find a ratio of 1×10^{-4} . Analyzing a sample of 98 Galactic clouds with *Planck* observations, Planck Collaboration et al. (2014b) derived a ratio of 2.5×10^{-4} . Thus, the AME component identified by Planck Collaboration et al. (2015b) has a strength relative to the $100 \mu\text{m}$ dust emission in good agreement with what has been observed in other studies.

However, as discussed in detail by Tibbs et al. (2012), this ratio is subject to significant variability. While the $100 \mu\text{m}$ emission is a reasonable proxy for the total dust luminosity, its sensitivity to the dust temperature introduces significant non-linearities in the relationship. This effect is evident in Figure 2d in the non-linear shape of the $100 \mu\text{m}$ scatter plot.

4.4. Correlation with $I_{\nu}^{12 \mu\text{m}}$

Finally, we find that the $12 \mu\text{m}$ emission is also tightly correlated with the AME with dispersion comparable to that of \mathcal{R} . While it is tempting to read this as a vindication of the spinning PAH model, the foregoing analysis

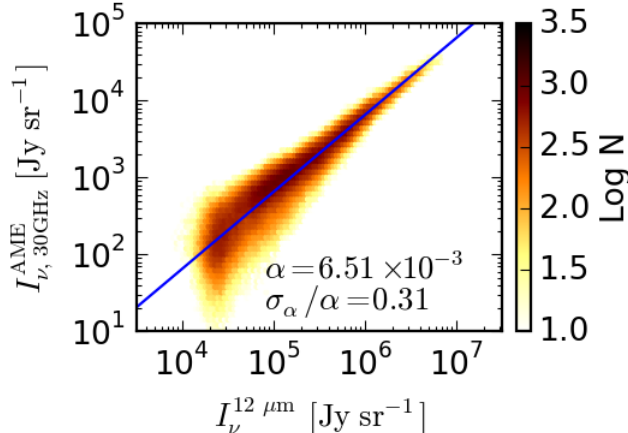


FIG. 6.— As in each panel of Figure 2, we plot the WISE 12 μm intensity against the 30 GHz AME intensity. The correlation is comparably tight as observed with \mathcal{R} .

suggests that this tight correlation is merely the product of the 12 μm emission being an excellent tracer of both the dust column and the radiation field strength. f_{PAH} , i.e. the 12 μm emission per unit \mathcal{R} , does not correlate with the AME intensity (see Figures 3 and 7).

Thus, while the PAH emission is an excellent predictor of the AME strength, this appears to be by virtue of being an excellent predictor of the dust radiance rather than the result of an inherent link between the AME and PAHs.

4.5. Emission from Magnetic Dust

If the AME is not spinning PAHs, could it be emission from magnetic grains? Draine & Lazarian (1999) predicted that, unlike spinning PAH emission, magnetic dust emission would be equally strong per dust mass in both dense and diffuse regions. Since the dust in dense regions will be cooler than that in diffuse regions, pixels with significant dust emission from both diffuse and dense regions will have broader SEDs and thus are fitted by smaller values of β relative to diffuse regions when fitting the SED with a modified blackbody. Thus, the AME per dust mass is predicted to be *negatively* correlated with β in the spinning PAH model and uncorrelated in the magnetic dust model. In Figure 5b we demonstrate that these quantities are largely uncorrelated ($r_s = 0.09$).

4.6. Dependence on Masks

The lack of correlation between f_{PAH} and the AME intensity per τ_{353} is a potentially serious problem for the spinning PAH hypothesis. We thus test the sensitivity of this result to the region of the Galaxy examined. In Figure 7, we perform the same analysis as in Figure 3a and quantify the degree of correlation with the Spearman correlation coefficient r_s .

Starting with the pixels remaining unmasked following the cuts discussed in 2.5, in Figure 7a we consider only the pixels at high Galactic latitude with $|b| > 15^\circ$. The behavior very much mimics that observed in Figure 3a, having if anything a *negative* correlation between f_{PAH} and the AME intensity per τ_{353} . In Figure 7b, we examine pixels with $|b| < 15^\circ$. These pixels have more PAH emission per dust radiance than those at higher latitudes.

Again, however, there is no indication of a correlation of the AME intensity per τ_{353} with f_{PAH} .

We next examine in Figure 7c only those pixels in which one or both of the AME components are significant at greater than 5σ . The cut on AME significance does not change significantly the behavior observed in Figure 7a other than to eliminate many pixels with low f_{PAH} values. As illustrated in Figure 4, the pixels with low f_{PAH} also tend to have low surface brightness. Finally, Figure 7d shows for comparison the same analysis performed on the standard mask (Figure 3a).

The non-correlation of the AME intensity and f_{PAH} is therefore robust to assumptions either on the AME significance or the region of the sky analyzed. We now turn to the implications of this result in the following section.

5. DISCUSSION

One of the largest sources of uncertainty in this analysis is the fidelity of the AME spectrum recovered from decomposition. Due to a lack of data between the WMAP 23 GHz band and the Haslam data at 408 MHz, it is difficult to constrain the relative contributions of the AME, synchrotron, and free-free in the frequency range of interest. Planck Collaboration et al. (2015b) notes that their estimates of synchrotron emission are lower than the 9 yr. WMAP analysis (Bennett et al. 2013) by about 70% at high Galactic latitudes and factors of several in the Galactic plane, with the AME component estimate being larger as a result. It is therefore possible that the AME map has a non-negligible synchrotron component.

The presence of contamination in the AME map, such as free-free or synchrotron, will of course mean that f_{PAH} is not related to the inferred AME intensity in a perfectly linear way even if the AME comes from spinning PAHs. Further, since f_{PAH} correlates with τ_{353} , it is also expected to correlate with the free-free and synchrotron emission, which increase with increasing gas (and therefore dust) column density.

As illustrated in Figure 8a, $I_\nu^{\text{AME}}/\tau_{353}$ has no appreciable correlation with the 30 GHz free-free emission per τ_{353} ($r_s = 0.01$). We therefore expect contamination from free-free to be minimal.

In Figure 8b, we plot $I_\nu^{\text{AME}}/\alpha\tau_{353}$ against the 30 GHz synchrotron intensity per τ_{353} . The two quantities show clear evidence of a positive correlation. In Figure 5c, we demonstrated that $I_\nu^{\text{AME}}/\tau_{353}$ is negatively correlated with τ_{353} . $I_\nu^{\text{sync}}/\tau_{353}$ also has a strong negative correlation with τ_{353} – the synchrotron is most dominant in diffuse regions. Thus, the positive correlation between $I_\nu^{\text{AME}}/\tau_{353}$ and $I_\nu^{\text{sync}}/\tau_{353}$ was to be expected.

For this analysis, a crucial question is whether synchrotron contamination is driving the negative correlation between $I_\nu^{\text{AME}}/\tau_{353}$ and τ_{353} . If this were the case, the same effect would be observed between $I_\nu^{\text{AME}}/\mathcal{R}$ and \mathcal{R} since $I_\nu^{\text{sync}}/\mathcal{R}$ behaves in the same manner as $I_\nu^{\text{sync}}/\tau_{353}$. However, we find that $I_\nu^{\text{sync}}/\mathcal{R}$ has if anything a negative correlation with $I_\nu^{\text{AME}}/\mathcal{R}$ ($r_s = -0.11$), suggesting that a synchrotron contribution to the estimated AME intensity is minimal.

Even assuming no contamination in the fit AME component, correlations with the synchrotron emission are plausible. For instance, if the AME arises from spinning

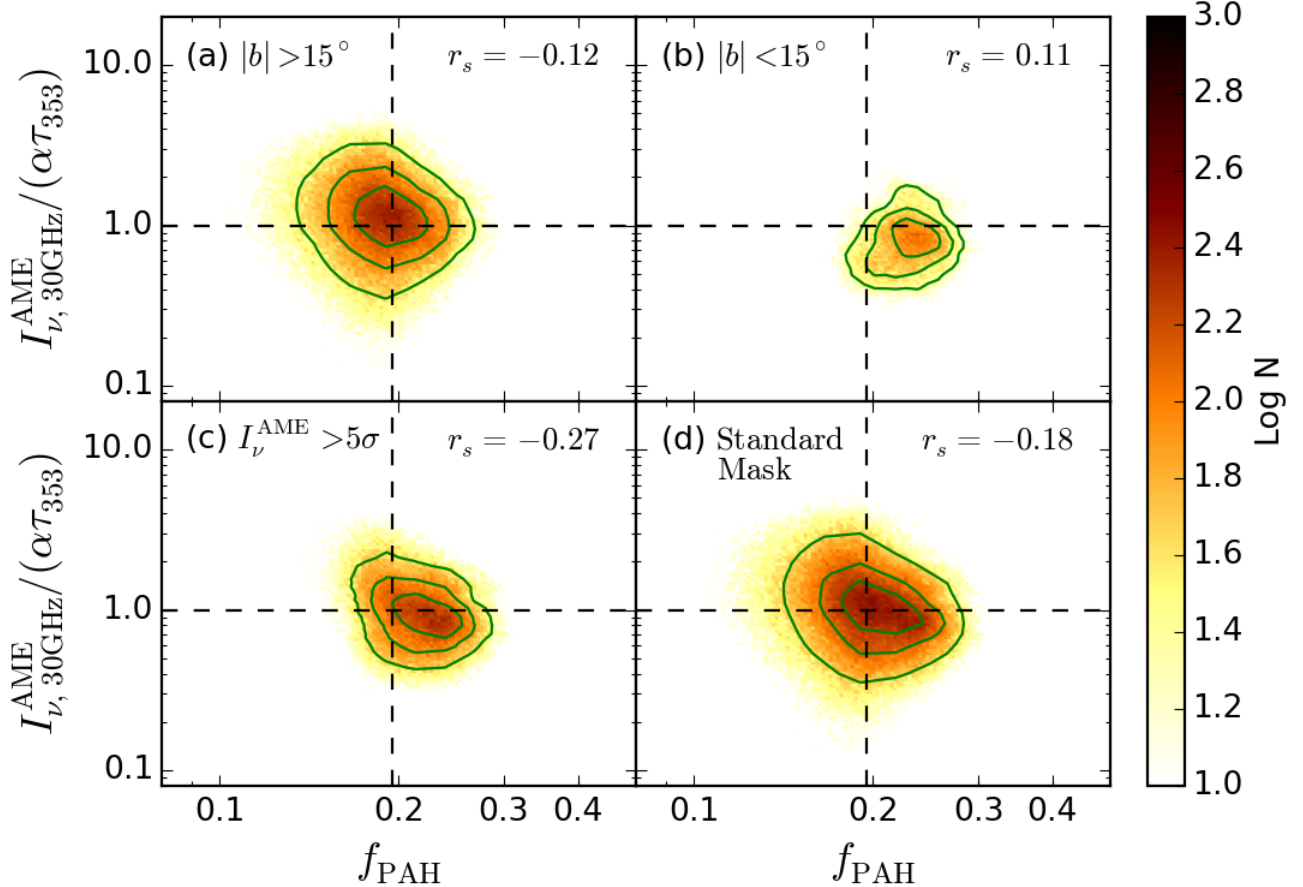


FIG. 7.— As in Figure 3, f_{PAH} is plotted against the 30 GHz AME intensity normalized by $\alpha\tau_{353}$. We examine four different masks: (a) considering only high Galactic latitudes $|b| > 15^\circ$, (b) considering only low Galactic latitudes $|b| < 15^\circ$, (c) considering only pixels in which at least one AME component was significant at $> 5\sigma$, and (d) using the standard mask only. For reference, the dashed lines mark the median values in the standard mask. In all cases, there is no evidence for correlation between the AME and f_{PAH} .

ulrasmall grains, it might be enhanced in regions such as supernova remnants in which grains are violently shattered and which have appreciable synchrotron emission, or perhaps suppressed as the result of the destruction of ulrasmall grains by sputtering.

The theoretical uncertainties in the models for these emission components underscore the need for obtaining ancillary data at lower frequency. Upcoming 5 GHz observations from the C-Band All-Sky Survey (C-BASS) (King et al. 2014) and 2.3 GHz observations from the S-Band Polarized All-Sky Survey (S-PASS) (Carretti et al. 2009) will play an invaluable role in disentangling the low-frequency components.

A second source of uncertainty is the ability of the $12\mu\text{m}$ emission to trace the PAH abundance. In particular, it can depend on the ionization state of the PAHs and other properties of the local environment (e.g. Draine & Li 2007). However, this would only add scatter to the expected relation – fluctuations in the $12\mu\text{m}$ emission would still be expected to correlate positively with fluctuations in the AME intensity as long as there is any ability whatsoever of the $12\mu\text{m}$ emission to trace the PAH abundance.

If indeed the AME is *not* correlated with the $12\mu\text{m}$ emission and *is* correlated with the strength of the radiation field, what are the implications for the origin of the emission? We present three possibilities:

1. The AME is spinning dust emission that arises primarily from ulrasmall grains that are not PAHs. Li & Draine (2001) have shown that as much as $\sim 10\%$ of the interstellar silicate mass could be in ulrasmall grains. However, it remains to be seen whether these grains could produce enough rotational emission to account for the AME.

2. The AME is only partially emission from spinning PAHs, but has a significant component from other sources, such as non-PAH spinning dust or thermal dust emission such as magnetic dipole emission. However, unless the spinning PAH contribution is quite small, this does not explain the lack of correlation between the AME and f_{PAH} .

3. The AME is predominantly thermal dust emission, such as magnetic dipole emission from magnetic materials. However, current models of magnetic dipole emission do not predict behavior that could emulate the observed AME SED without invoking extreme grain geometries (Draine & Hensley 2013). More laboratory data is needed to assess the behavior of magnetic materials at microwave frequencies to determine whether such grains could be a potential source of the AME. It remains conceivable that some interstellar grain component might produce the AME by non-rotational electric dipole radiation, but we are not aware of materials that could do this.

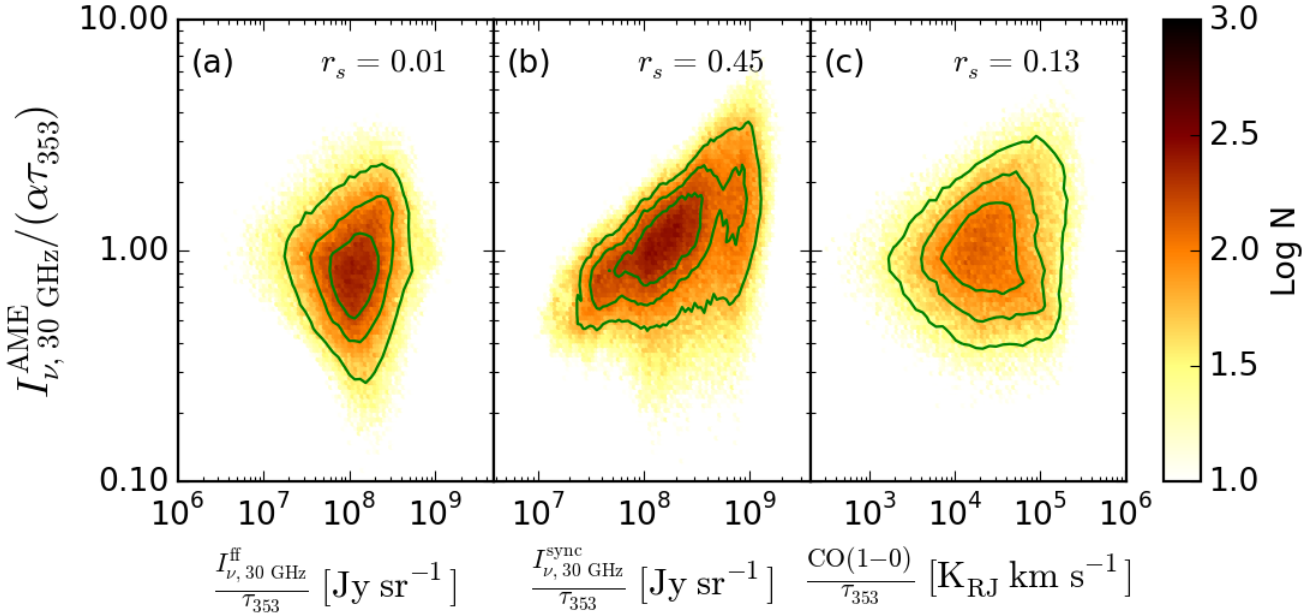


FIG. 8.— The 30 GHz AME intensity normalized by $\alpha\tau_{353}$ is plotted against (a) the 30 GHz free-free intensity, (b) the 30 GHz synchrotron intensity, and (c) the CO(1-0) line emission all normalized by τ_{353} . Although there is no evidence for strong correlations with free-free or CO emission, the AME per τ_{353} appears positively correlated with the synchrotron emission per τ_{353} . As discussed in Section 5, this does not appear driven by synchrotron contamination in the fit AME component but rather correlations between the synchrotron emission and the environments that favor or disfavor AME.

Invoking an alternative explanation for the AME also requires explaining why the PAHs are *not* a substantial source of spinning dust emission. Because the PAHs are clearly present and must be rotating, this would require that the electric dipole moments of the PAHs have been greatly overestimated (the spinning dust emission scales as the square of the dipole moment). The electric dipole moments of selected hydrocarbon molecules compiled by Draine & Lazarian (1998b) have a scatter of nearly an order of magnitude. Further, harsh UV irradiation more easily destroys asymmetric molecules, perhaps preferentially selecting for a population of more symmetric PAHs with smaller dipole moments. Thus it is plausible that the dipole moment distributions adopted in spinning dust models may significantly overestimate the true electric dipole moments of interstellar PAHs.

Lazarian & Draine (2000) estimated the polarization fraction of spinning dust emission to be $p \lesssim 0.01$ near 30 GHz. This estimate would also apply to spinning dust emission from non-PAH grains. However, if the AME is thermal emission from large aligned grains, it should be significantly polarized with $\vec{E} \parallel \vec{B}_0$ for electric dipole radiation or $\vec{E} \perp \vec{B}_0$ for magnetic dipole radiation from magnetic inclusions (Draine & Hensley 2013).

Observations of known AME sources in polarization suggest minimal polarization of the AME. In the Perseus molecular cloud, the polarization fraction was found to be $3.4^{+1.5}_{-1.9}\%$ at 11 GHz (Battistelli et al. 2006), less than 6.3% at 12 GHz (Génova-Santos et al. 2015), less than 2.8% at 18 GHz (Génova-Santos et al. 2015), and less than $\sim 1\%$ at 23 GHz (López-Caraballo et al. 2011; Dickinson et al. 2011). Likewise, observations of the ρ Ophiuchi molecular cloud have yielded upper limits of $\lesssim 1\%$ at 30 GHz (Casassus et al. 2008; Dickinson et al. 2011). Mason et al. (2009) placed an upper limit of 2.7% on the

9.65 GHz polarization fraction in the dark cloud Lynds 1622. 21.5 GHz observations of the HII region RCW175 yielded a polarization fraction of $2.2 \pm 0.3\%$ (Battistelli et al. 2015).

These upper limits on polarization in the 10 - 30 GHz emission appear to favor spinning dust emission from a non-PAH population of ultrasmall grains.

6. CONCLUSION

We have combined the *Planck* foreground component maps, *Planck* modified blackbody dust parameter maps, and WISE 12 μm maps to test key predictions of the spinning PAH hypothesis. The principal conclusions of this work are as follows:

1. τ_{353} , the dust radiance \mathcal{R} , and $I_{\nu}^{12\mu\text{m}}$ are all excellent predictors of the 30 GHz AME intensity. \mathcal{R} and $I_{\nu}^{12\mu\text{m}}$ exhibit the tightest correlation, suggesting that the AME is sensitive to the strength of the radiation field.
2. Neither the AME per τ_{353} nor AME per dust radiance \mathcal{R} show any correlation with the PAH emission whether considering the full sky, high Galactic latitudes, or regions closer to the Galactic plane.
3. Taken together, these facts pose a serious challenge to the spinning PAH paradigm as the explanation for the AME. Alternative explanations, such as magnetic dipole emission from ferro- or ferrimagnetic grains, should be more thoroughly investigated.
4. More low frequency constraints are needed to break degeneracies between the AME, free-free, and synchrotron to enable accurate decomposition and to better constrain the AME spectrum. Upcoming

all-sky observations from C-BASS and S-PASS will thus facilitate deeper investigations into the origin of the AME.

5. Further measurements of AME polarization will help clarify the nature of the grains responsible for

the AME.

We thank Aaron Meisner and Doug Finkbeiner for assistance with the 12 μ m maps, and Chelsea Huang, David Spergel, and Chris White for stimulating conversations. BSH and BTD acknowledge support from NSF grant AST-1408723.

REFERENCES

Ali-Haïmoud, Y., Hirata, C. M., & Dickinson, C. 2009, MNRAS, 395, 1055

Alves, M. I. R., Davies, R. D., Dickinson, C., et al. 2010, MNRAS, 405, 1654

Battistelli, E. S., Rebolo, R., Rubiño-Martín, J. A., et al. 2006, ApJ, 645, L141

Battistelli, E. S., Carretti, E., Cruciani, A., et al. 2015, ApJ, 801, 111

Bennett, C. L., Larson, D., Weiland, J. L., et al. 2013, ApJS, 208, 20

Carretti, E., Gaensler, B., Staveley-Smith, L., et al. 2009, S-band Polarization All Sky Survey (S-PASS), ATNF Proposal

Casassus, S., Cabrera, G. F., Förster, F., et al. 2006, ApJ, 639, 951

Casassus, S., Dickinson, C., Cleary, K., et al. 2008, MNRAS, 391, 1075

Davies, R. D., Dickinson, C., Banday, A. J., et al. 2006, MNRAS, 370, 1125

de Oliveira-Costa, A., Kogut, A., Devlin, M. J., et al. 1997, ApJ, 482, L17

Dickinson, C., Peel, M., & Vidal, M. 2011, MNRAS, 418, L35

Dobler, G., Draine, B., & Finkbeiner, D. P. 2009, ApJ, 699, 1374

Dong, R., & Draine, B. T. 2011, ApJ, 727, 35

Draine, B. T., & Hensley, B. 2013, ApJ, 765, 159

Draine, B. T., & Lazarian, A. 1998a, ApJ, 494, L19

—. 1998b, ApJ, 508, 157

—. 1999, ApJ, 512, 740

Draine, B. T., & Li, A. 2007, ApJ, 657, 810

Eriksen, H. K., Jewell, J. B., Dickinson, C., et al. 2008, ApJ, 676, 10

Eriksen, H. K., O'Dwyer, I. J., Jewell, J. B., et al. 2004, ApJS, 155, 227

Eriksen, H. K., Dickinson, C., Lawrence, C. R., et al. 2006, ApJ, 641, 665

Foreman-Mackey, D., Hogg, D. W., Lang, D., & Goodman, J. 2013, PASP, 125, 306

Génova-Santos, R., Rubiño-Martín, J. A., Rebolo, R., et al. 2015, ArXiv e-prints, arXiv:1501.04491

Górski, K. M., Hivon, E., Banday, A. J., et al. 2005, ApJ, 622, 759

Haslam, C. G. T., Salter, C. J., Stoffel, H., & Wilson, W. E. 1982, A&AS, 47, 1

Hensley, B., Murphy, E., & Staguhn, J. 2015, MNRAS, 449, 809

Hoang, T., Draine, B. T., & Lazarian, A. 2010, ApJ, 715, 1462

Hoang, T., Lazarian, A., & Draine, B. T. 2011, ApJ, 741, 87

King, O. G., Jones, M. E., Blackhurst, E. J., et al. 2014, MNRAS, 438, 2426

Kogut, A., Banday, A. J., Bennett, C. L., et al. 1996, ApJ, 460, 1

Lazarian, A., & Draine, B. T. 2000, ApJ, 536, L15

Leitch, E. M., Readhead, A. C. S., Pearson, T. J., & Myers, S. T. 1997, ApJ, 486, L23

Li, A., & Draine, B. T. 2001, ApJ, 550, L213

López-Caraballo, C. H., Rubiño-Martín, J. A., Rebolo, R., & Génova-Santos, R. 2011, ApJ, 729, 25

Mason, B. S., Robishaw, T., Heiles, C., Finkbeiner, D., & Dickinson, C. 2009, ApJ, 697, 1187

Meisner, A. M., & Finkbeiner, D. P. 2014, ApJ, 781, 5

Miville-Deschénes, M.-A., & Lagache, G. 2005, ApJS, 157, 302

Miville-Deschénes, M.-A., Ysard, N., Lavabre, A., et al. 2008, A&A, 490, 1093

Murphy, E. J., Helou, G., Condon, J. J., et al. 2010, ApJ, 709, L108

Planck Collaboration, Abergel, A., Ade, P. A. R., et al. 2014a, A&A, 571, A11

Planck Collaboration, Ade, P. A. R., Aghanim, N., et al. 2014b, A&A, 565, A103

Planck Collaboration, Abergel, A., Ade, P. A. R., et al. 2014c, A&A, 566, A55

Planck Collaboration, Adam, R., Ade, P. A. R., et al. 2015a, ArXiv e-prints, arXiv:1502.01582

—. 2015b, ArXiv e-prints, arXiv:1502.01588

Plank Collaboration, Ade, P. A. R., Aghanim, N., et al. 2014, ArXiv e-prints, arXiv:1409.2495

Scaife, A. M. M., Nikolic, B., Green, D. A., et al. 2010, MNRAS, 406, L45

Schlegel, D. J., Finkbeiner, D. P., & Davis, M. 1998, ApJ, 500, 525

Silsbee, K., Ali-Haïmoud, Y., & Hirata, C. M. 2011, MNRAS, 411, 2750

Tibbs, C. T., Paladini, R., & Dickinson, C. 2012, Advances in Astronomy, 2012, arXiv:1212.3269

Tibbs, C. T., Watson, R. A., Dickinson, C., et al. 2010, MNRAS, 402, 1969

Tibbs, C. T., Flagey, N., Paladini, R., et al. 2011, MNRAS, 418, 1889

Todorović, M., Davies, R. D., Dickinson, C., et al. 2010, MNRAS, 406, 1629

Wright, E. L., Eisenhardt, P. R. M., Mainzer, A. K., et al. 2010, AJ, 140, 1868

Ysard, N., Miville-Deschénes, M. A., & Verstraete, L. 2010, A&A, 509, L1

Ysard, N., & Verstraete, L. 2010, A&A, 509, A12